Capillarity Vol. 17, No. 3, p. 97-108, 2025

Original article

The mechanism of capillaries hydraulic conductivity evolution under confining pressure: Experimental modelling using 3D-printing approach

Evgenii Riabokon[1]*, Mikhail Turbakov[1], Evgenii Kozhevnikov[1], Dmitrii Kobiakov[1], Zakhar Ivanov[2], Mikhail Guzev[1], Liyuan Yu[3]

[1] *Department of Oil and Gas Technologies, Perm National Research Polytechnic University, Perm 614990, Russia*

[2] *Laboratory of natural gas hydrates, Perm National Research Polytechnic University, Perm 614990, Russia*

[3] *State Key Laboratory of Intelligent Construction and Healthy Operation and Maintenance of Deep Underground Engineering, China University of Mining and Technology, Xuzhou 221116, P. R. China*

Keywords:
Capillary conductivity
capillary deformation
additive technologies
three-dimensional-printing
capillary hydraulic area

Cited as:
Riabokon, E., Turbakov, M., Kozhevnikov, E., Kobiakov, D., Ivanov, Z., Guzev, M., Yu, L. The mechanism of capillaries hydraulic conductivity evolution under confining pressure: Experimental modelling using 3D-printing approach. Capillarity, 2025, 17(3): 97-108.
https://doi.org/10.46690/capi.2025.12.03

Abstract:
The effect of confining pressure on the hydraulic conductivity of capillaries in cylindrical samples is examined. The three-dimensional-printed samples were made from photopolymer resin. Capillaries in the samples were modeled by grooves of various geometric shapes. The mechanism of capillary deformation in the samples under increasing confining pressure has been identified. The change in capillary conductivity depending on their location (central and lateral) and configuration (sinuous) has been revealed. Based on correction functions for the geometric dimensions of the capillaries, it has been mathematically confirmed that under confining pressure, a capillary deforms primarily along the contact plane due to the sliding of the sample's halves against each other. The width of a capillary is more sensitive to confining pressure than its depth. It has been established that the exponent in the conductivity (permeability) equation of the samples under cyclic loading is determined by the hydraulic area of the capillary. The obtained values of the width and depth correction factors allow for predicting changes in the filtration resistances of capillaries in various materials. Capillary deformation manifests as a change in its geometric dimensions (height and width), i.e., the crushing of the capillary banks is observed, leading to a reduction in the capillary's hydraulic area, which causes a decrease in sample conductivity with an incomplete hysteresis.

---

1. Introduction

The permeability of channels (fractures or capillaries) in deformable media is a critically important parameter studied in various fields, including medicine (e.g., muscle contraction) (Planas-Paz and Lammert, 2013), bioengineering (e.g., cartilage biomechanics) (Eschweiler et al., 2021; Petitjean et al., 2022), membranes (Persson et al., 1995; Dawson et al., 2007; Aghajani et al., 2017), and fuel cells (Khetabi et al., 2019). In the context of rock mass, the width of a fracture opening, known as its aperture, is a critical parameter influencing key engineering applications such as naturally fractured reservoir dynamics (Paluszny and Matthai, 2010; Boro et al., 2014; Fan et al., 2015), drilling operations (Al

---

*Corresponding author.
E-mail address: riabokon@pstu.ru (E. Riabokon); msturbakov@pstu.ru (M. Turbakov); kev@pstu.ru (E. Kozhevnikov); kobiakovdv@gmail.com (D. Kobiakov); zakharivanov@pstu.ru (Z. Ivanov); guzev@iam.dvo.ru (M. Guzev).
Yandy Scientific Press
2709-2119
Received October 20, 2025; revised November 23, 2025; accepted December 12, 2025; available online December 15, 2025.

Mteiri et al., 2020), hydraulic fracturing (Yang et al., 2018; Gehne and Benson, 2019; Wei et al., 2024), enhanced oil recovery (Poplygin et al., 2024), well remedial cementing (Ketova, 2017), carbon dioxide sequestration (Xue et al., 2025) and groundwater resource management (Ouf et al., 2024). In geotechnical engineering, conductivity is also a key parameter in soil improvement projects for ground dewatering using prefabricated vertical drains (or wick drains) (Kamal et al., 2025; Kuganeswaran et al., 2021). An increase in vertical pressure (due to soil compaction) leads to greater radial pressure on the wick drains, resulting in reduced channel permeability (Tran-Nguyen et al., 2010; Bo et al., 2016). Furthermore, channel permeability is also an important parameter in the field of microfluidics (Ma et al., 2025).

In some extent fractures in rocks are similar to capillaries. It is known that an increase in confining pressure leads to a reduction in the aperture of capillaries within the material and, consequently, a decrease in fluid flow through the fracture (Kozhevnikov et al., 2023). As noted in (Bandis et al., 1983), understanding the deformation response of rock joints is critical for assessing rock permeability. Shear fractures in rock masses are the main channels for the filtration of formation waters. The study (Kim and Inoue, 2003) demonstrated that the permeability of shear fractures is predominantly influenced by the roughness of the fracture surfaces and its alteration due to shear. Among the known constitutive laws describing fracture deformation are the models by Goodman (1974), Bandis et al. (1983), Sun and Lin (1983) and Rong et al. (2011). The work (Feng et al., 2023) notes that for water filtration through a cylindrical shale sample, cut lengthwise, the relationship between confining pressure, hydraulic aperture, and flow rate is most accurately described by the Sun model. Furthermore, it is often the case that after applying the confining pressure, the rocks are in a state of hydrostatic pressure, and the pre-existing cracks are closed (Zuo et al., 2019).

In the study of flow capacity, the cubic law has found widespread application. This law states that the flow rate of a fluid through a fracture consisting of parallel plates is proportional to the cube of the fracture aperture (Witherspoon et al., 1980). However, a different approach is required for channels with constrained geometric dimensions. Hydraulic conductivity (like permeability) characterizes the ability of a porous medium to transmit fluid. Unlike permeability, however, conductivity accounts for the hydraulic head (hydraulic gradient) and is measured in units of velocity, such as centimeters per second (see, for example, Goodman, 1989, Section 2.5).

The most common manifestation of the phenomenon of changing filtration characteristics of rocks is the reduction of rock permeability during the development of hydrocarbon fields (Vogler et al., 2016; Kluge et al., 2021), coal mining (Wang et al., 2022), and underground construction (Zhou et al., 2020).

It is generally accepted that the filtration characteristics (permeability or conductivity) under load, including cyclic loads, decrease as a result of capillary closure (Kozhevnikov et al., 2023). The primary reason for the permeability reduction in fractured rocks is the compaction of the internal structure of the sample subjected to compression (Hofmann et al., 2016). However, the precise mechanism of how the capillary compaction process occurs in a cylindrical sample under confining pressure remains not fully understood. Since the capillary conductivity of the media is a viable characteristic therefore it is of particular interest to study the changes in capillary conductivity depending on confining pressure.

The advancement of additive technologies (such as 3D printing) allows for the experimental demonstration of capillary deformation processes inside a cylindrical sample (Ibrahim et al., 2021; Azin et al., 2025). Using 3D-printed samples of the rock plug size, this article investigates the influence of changes in the geometric dimensions of capillaries inside a sample on the sample's filtration characteristics (conductivity). The article is structured as follows. Section 2 describes the materials and methods used in the study. Section 3 presents the results of the experimental and analytical research and their discussion. The conclusions are provided in Section 4.

2. Materials and methods

The stereolithography (SLA) technology was used to fabricate the model samples, as SLA printing is widely employed in geosciences, particularly for producing porous and capillary rock replicas (Chen et al., 2023; Almubarak et al., 2024). The sample size is 30 mm in diameter and 30 mm in length. The material for the models was photopolymer resin, which hardens layer by layer when exposed to ultraviolet light. During the 3D-printing of a cylindrical sample with an internal capillary, the solidification process of the sample can lead to the deformation of porous structures (adhesion of the capillary walls), which prevents maintaining the specified capillary geometry. To address this issue and study the deformation behavior of the rock under load for samples with defined capillary geometries, a methodology for manufacturing a 3D-sample model was developed. According to this methodology, the cylinder is fabricated as two separate halves to ensure the capillary's integrity. One half is solid, while the other has a groove on the contact surface with the first half (Fig. 1(a)). The shape of the groove is shown in Fig. 1(b)). In this study, a capillary is modeled by a groove with a specified depth and width. The capillary acts as a physical model of the sample's pore space through which filtration occurs. To minimize scattering effects during printing, the capillary has a rectangular shape (Fig. 1(b)). The samples were printed with supports, oriented with the capillary facing the display (Fig. 1(c)).

The manufacturing process involves creating a digital model (Figs. 1(a) and 1(b)), preparing the digital model for printing-specifically by arranging support structures designed to prevent model deformation during printing-and subsequent printing (Fig. 1(c)). After the printed models were removed, they were cleaned of residual resin by placing them in an ultrasonic bath with isopropyl alcohol. Following printing, the capillaries were inspected for defects and contaminants using a microscope (Fig. 1(e)). If necessary, the capillaries were cleaned using a soft-bristled brush, which is incapable

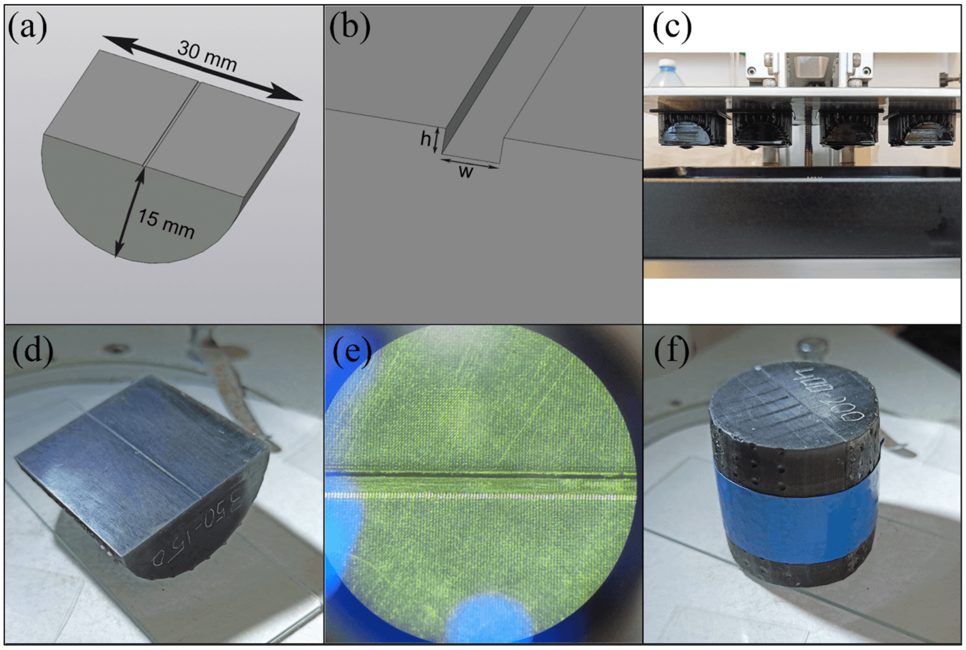

Fig. 1. Stages of manufacturing a 3D-printed sample with a capillary in the middle: (a) shape and dimensions of the model half, (b) capillary shape, (c) samples on the 3D-printer during printing, (d) printed half of the sample with a capillary, (e) micrograph of the sample with a capillary and (f) assembled 3D-printed sample consisting of two halves with a capillary inside.

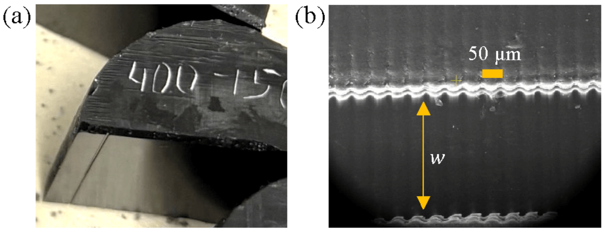

Fig. 2. Sample with a (a) laterally located straight capillary (Type B) and (b) microcapillary.

of damaging the main body of the model. The finished half of the sample is then assembled with the half without a capillary to conduct filtration studies.

Four types of 3D-printed samples were manufactured: (A) samples with a centrally located straight capillary and a smooth contact surface (Fig. 1(d)), (B) samples with a laterally located straight capillary and a smooth contact surface (Fig. 2), (C) samples with a centrally located sinuous capillary and a smooth contact surface (Fig. 3).

To obtain the relationships between capillary conductivity and deformation, a series of samples with 12 different width and height combinations were manufactured. Each combination gave the 3D-printed sample a unique initial capillary conductivity. The groove characteristics are presented in Table 1. In total, over 70 samples with capillaries of different sizes, shapes, locations, and contact surface configurations were manufactured for the study to simulate sliding during deformation and the closure of relaxation cracks (Fig. 4).

After printing, the samples were visually inspected for surface smoothness (Fig. 1(d)) and capillary cleanliness (Fig. 1(e)). Subsequently, the assembled model (Fig. 1(f)) was placed in the core holder of the UltraPoroPerm-500 filtration setup. Filtration studies were conducted by injecting nitrogen according to the following procedure (Fig. 5). Using a manual pump (1), the 3D-printed sample (3) in the sample holder (2) was subjected to a confining pressure applied by a rubber sleeve. Using a gas flow regulator (4), nitrogen from a cylinder (6) was directed in a specified volume through a system of tubes into the 3D-printed sample (3). The personal computer (5) and the measurement system (7) were used to measure the pressure across the sample (3) between the inlet channel and the outlet channel. This recorded the pressure differential, which characterizes the flow resistance encountered during gas flow through the porous medium. More details on experimental set-up can be found in (Kozhevnikov et al., 2024).

Prior to conducting the filtration studies, tests were performed to verify the absence of nitrogen leakage along the contact plane between the two halves of the 3D-printed sample. For this purpose, two solid halves without grooves were assembled and placed in the core holder under a confining pressure of 2.76 MPa (400 psi). The test results confirmed that the sample composed of two solid halves was sealed at a nitrogen injection pressure of 0.7 MPa (101 psi). Thus, it was established that flow occurs exclusively within the capillary, and the presence of the contact surfaces and their configuration does not affect the accuracy of the obtained experimental data.

In order to ensure the laminar flow additional prior tests were conducted. Depending on the groove dimensions of the samples, a nitrogen flow rate from 0.16 to 1 cm^3/s corresponds to the linear flow regime. The plots (Fig. 6) show the pressure drop across the samples and the friction factor versus the Reynolds number (Re). The dependencies are linear at Re up to 100, which corresponds to laminar flow. Thus, despite the

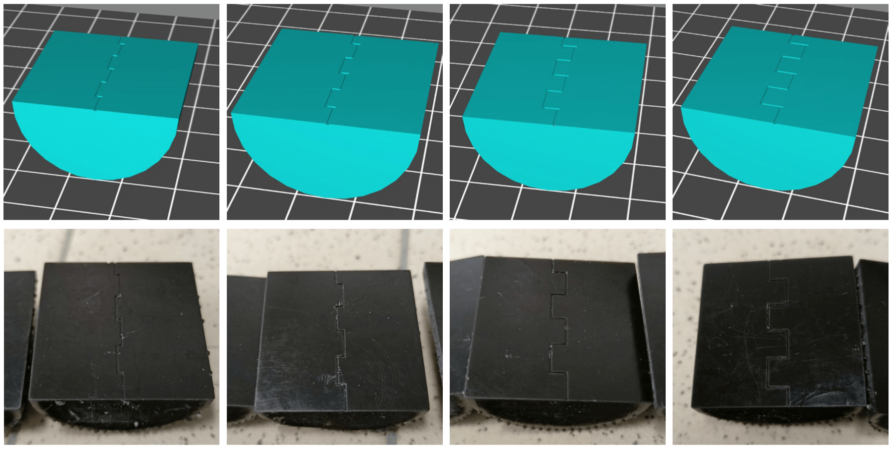

$T = 1.15$ $T = 1.225$ $T = 1.45$ $T = 1.6$

Fig. 3. 3D-models and 3D-printed samples with sinuous capillaries (Type B) and different tortuosity values T.

Table 1. Characteristics of the grooves in the 3D-printed samples.

Capillary characteristic	No.											
	1	2	3	4	5	6	7	8	9	10	11	12
Width w (μm)	300	300	250	350	350	400	450	350	450	400	400	450
Height h (μm)	100	150	200	100	150	100	100	200	150	150	200	200
Initial conductivity ($\times 10^{-5}$ cm^3/(sec$\cdot$Pa))	0.24	0.52	0.52	0.55	0.79	1.06	1.19	2.08	2.35	2.37	7.81	12.12

small filtration area compared to core samples, the laminar flow regime in the replicas is maintained at sufficiently high flow velocities for Re up to 100. In contrast, in a porous medium, due to its tortuosity, the transitional flow begins at Re from 10, and according to some data, from 1. The friction factor for laminar flow in replicas with a straight channel is described by the classical Blake-Kozeny equation: $\lambda = 150/\mathrm{Re}$ which corresponds to the friction factor for packed beds of identical spheres. For comparison, the graph (Fig. 6(b)) shows the calculated values from the experimental data and from the $\lambda = 150/\mathrm{Re}$ equation; the obtained values are in agreement. The friction factor is derived from the Darcy-Weisbach equation:

$$
\begin{aligned}
dP &= \Delta P_f = \lambda \frac{L}{D_h} \frac{\vartheta^2}{2} \rho \\
\lambda &= \Delta P_f \frac{D_h}{L} \frac{2}{\vartheta^2 \rho}
\end{aligned}
\tag{1}
$$

where L stands for groove length, mm; dP stands for differential pressure; P_f stands for friction losses, Pa; λ stands for friction coefficient; D_h stands for groove's diameter; ϑ stands for fluid velocity through the groove, m/s; ρ stands for fluid's density, kg/m^3).

Filtration tests were conducted at a constant nitrogen injection pressure under cyclic confining pressure according to the methodology proposed in (Kozhevnikov et al., 2024). Since the sample material (except the capillary itself) is non-porous and nitrogen flows exclusively through the capillary, conductivity was chosen as the convergence criterion instead of permeability. The instantaneous nitrogen conductivity of the samples was determined experimentally as the ratio of the measured nitrogen flow rate, accounting for compressibility, to the measured pressure gradient across the sample, using the formula:

$$
C = \frac{Q}{(P_{\mathrm{in}}^2 - P_o^2)/P_o L} \tag{2}
$$

where Q stands for measured nitrogen flow rate, cm^3/s; P_{in} stands for measured nitrogen injection pressure, Pa; P_o stands for measured outlet pressure, Pa.

In order to assess the changes in the conductivity of capillaries in various material, taking their deformation into account, the methodology was developed which consists of the following steps: (i) Creating 3D-printed samples with varying capillary locations and configurations, (ii) performing cyclic and flow experiments, (iii) identifying the discrepancy between the theoretical and experimental conductivity of the samples, (iv) determining adjustment functions that reflect the actual deformation of the capillary, (v) obtaining the actual capillary conductivity as a power function of the load. The results given in the following Section 3 were obtained using the methodology hereabove.

The numerical simulation was done in ANSYS package based on the following input parameters. Isotropic elasticity was derived from Young's modulus and Poisson's ratio (Table 2). Mesh detail is given in Table 2. Boundary conditions are

Fig. 4. 3D-printed samples.

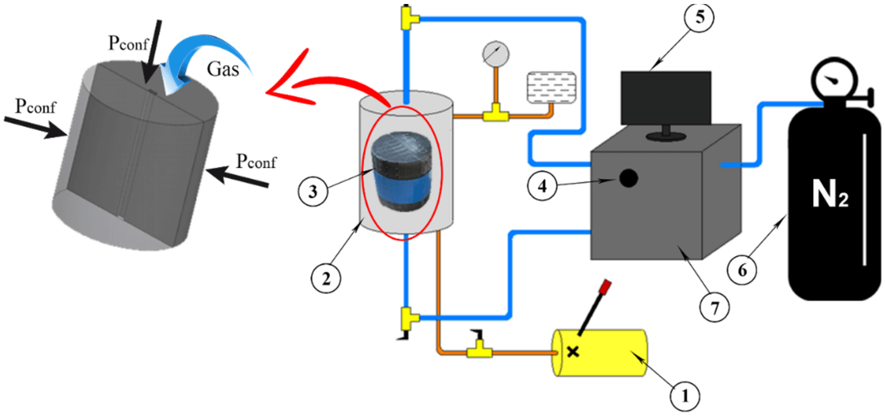

Fig. 5. Schematics of the core model testing setup: (1) Manual pump for maintaining confining pressure, (2) sample holder, (3) 3D-printed sample, (4) nitrogen flow regulator, (5) computer, (6) nitrogen cylinder, and (7) measurement system.

given in Table 2.

3. Results and discussion

Before analyzing the results obtained from the experimental modeling, it should be noted that the cyclic loading of the 3D-printed samples is performed within their linear elastic regime (corresponding to the quasi-elastic zone identified in Kozhevnikov et al. (2025)). In that regime stress and strain are linearly related by Young's modulus. The study (Kozhevnikov et al., 2025) also showed that Young's modulus values range from 3,893 MPa for a sample with a layer orientation of 60° to 4,272 MPa for a sample with layers parallel to the load. The elasticity of the samples is clearly demonstrated in the experiments to determine hydraulic conductivity under cyclic loading. As can be seen from Fig. 7, three load-unload cycles were applied to the sample by the rubber sleeve. The confining pressure was discretely increased from 3 to 14 MPa. The increase in sample confining pressure corresponds to a measured decrease in capillary conductivity from 2.25×10^{-5} to 1.85×10^{-5} $\mathrm{cm}^3/(\mathrm{s \cdot Pa})$ on the filtration setup.

The complete recovery of conductivity after the second and third load-unload cycles to the level observed after the first cycle indicates elastic deformation of the sample and the return of the capillary's geometric dimensions to their original values. Thus, all effects observed in the experiment are studied within the regime of elastic deformation, without failure.

3.1 Schematic of elastic groove deformation

A schematic representation of capillary deformation is shown in Fig. 8. In the case of a centrally located capillary (Fig. 8(a)), an increase in sample confining pressure leads to a reduction in the vertical dimensions of the capillary. Due to frictional forces between the halves, the capillary banks (walls) are drawn towards the center of the sample, forming an isosceles trapezoid. In the case of a laterally located capillary (Fig. 8(b)), the capillary banks converge asymmetrically (unlike the central placement), forming a trapezoid whose edge farther from the center has a greater inclination compared to the edge closer to the center. This is due to the greater deformation of the outer part of the sample.

Frictional forces F_{fric}, elastic forces F_{elast} and confining forces F_{conf} are the key factors determining capillary deformation. In the case of a centrally located capillary, the sample material provides uniform horizontal support around the capillary. When confining pressure is absent $F_{conf} = 0$, the capillary maintains a rectangular shape (Fig. 9(a)), and its walls are perpendicular to the base. When confining pressure is applied and increased, compressive stresses along the plane of the capillary exceed the elastic restoring forces $F_{conf} > F_{elast}$. The lack of material support in the capillary region leads to an elastic inward displacement of the capillary walls toward the sample's axis. Simultaneously, frictional forces between the halves slightly resist the wall convergence (Fig. 9(b)), acting

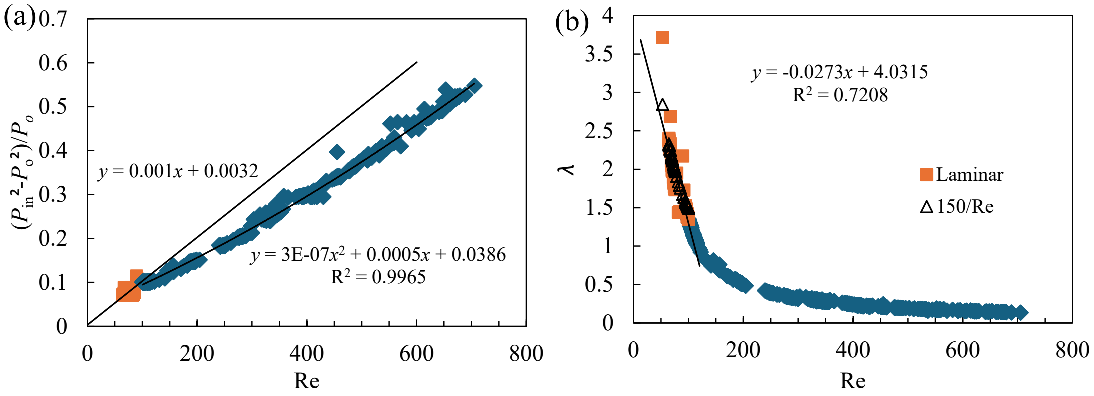

Fig. 6. Accounting for (a) nitrogen compressibility pressure drop and (b) friction factor as a function of Re.

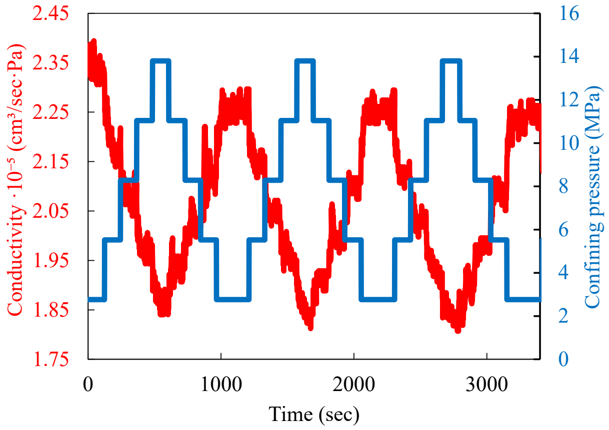

Fig. 7. The effect of confining pressure on the conductivity of a capillary in a 3D-printed sample.

in the opposite direction. When confining pressure is decreased, the frictional forces hinder the walls from returning fully to their initial position (Fig. 9(c)). In the case of a laterally located capillary, the developed radial stresses are non-uniform. Consequently, the deformation is more pronounced on the far bank of the capillary (the one farther from the center).

During the experiment, it was established that the dimensions of the capillary under confining pressure in the core holder differ from their initial dimensions. For each sample, the maximum and minimum conductivity values over the entire testing period were identified. The graphs show the maximum and minimum conductivity of the samples under cyclic loading versus the hydraulic area of the grooves (Fig. 10). It was found that the conductivity values can be conditionally divided into three clusters, each corresponding to a specific capillary depth h.

3.2 Adjustment of capillary dimensions under uniaxial loading

Since the conductivity values of the grooves obtained from the model differ from the values obtained experimentally, an adjustment of the geometric dimensions (width Δw and depth Δh) of the grooves was performed. This correction accounts for their location (central and lateral) and configuration (sinuous), without considering cyclic loading. The proportions of the residual width Δw and depth Δh of the grooves were determined using the formulas:

Table 2. Parameters.

Type	Parameter	Value
Material	Diameter (mm)	30
	Length (mm)	30
	Model parts (-)	2 half-cylinders
	Young's modulus (GPa)	1.55
	Poisson's ratio (-)	0.4
	Bulk modulus (GPa)	2.58
	Shear modulus (MPa)	0.55
Mesh	Groove cross-section width (mm)	0.45
	Boundary box (-)	51.962
	Average surface (mm^2)	504.24
	Minimum edge size (mm)	0.2
	Span angle center (-)	Coarse
Boundary conditions	Displacement	$\Delta x = 0$ in any direction
	Confining pressure	400-800-1200-1600-2000 psi (2.76-13.8 MPa)

$$\Delta w = \frac{w_{cor}}{w} \tag{3}$$

$$\Delta h = \frac{h_{cor}}{h} \tag{4}$$

where w_{cor} and h_{cor} are corrected groove width and depth, m; w and h represent initial width and depth, m.

Using the adjusted groove dimensions, the dependencies of conductivity on the adjusted hydraulic area of the grooves were obtained (Fig. 11), as well as the dependencies of the calculated residual width (Fig. 12(a)) and depth (Fig. 12(b))

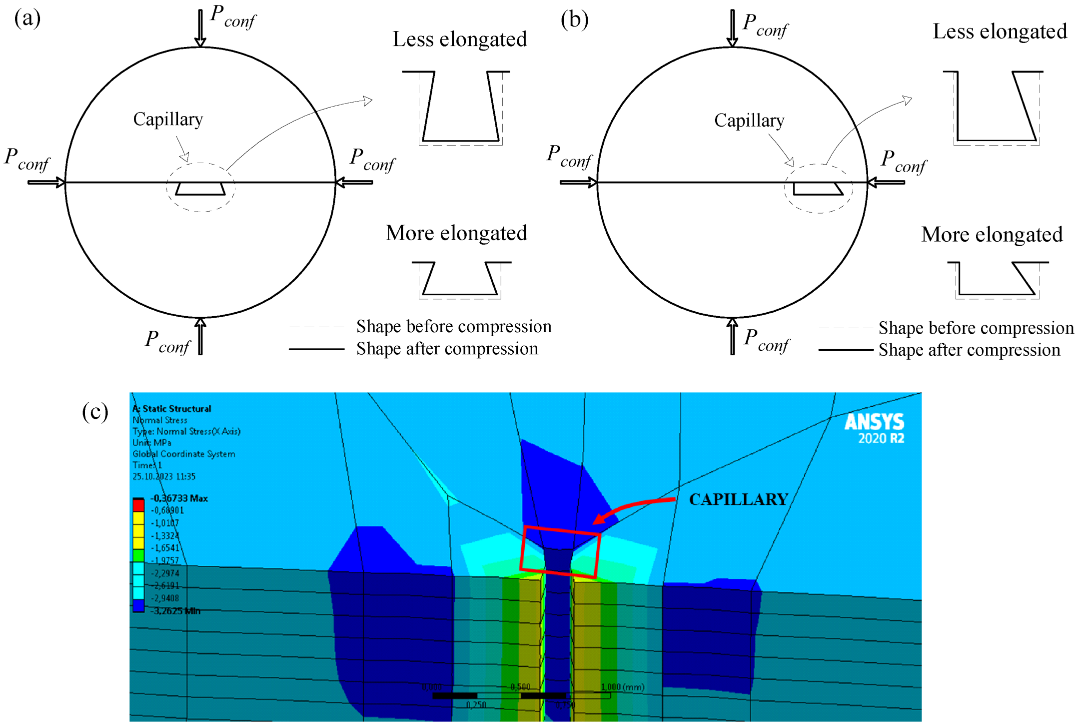

Fig. 8. Capillary geometry change under confining pressure change for a capillary located: (a) In the center of the sample, (b) on the side of the sample, and (c) in the center of the sample modelled in Ansys package.

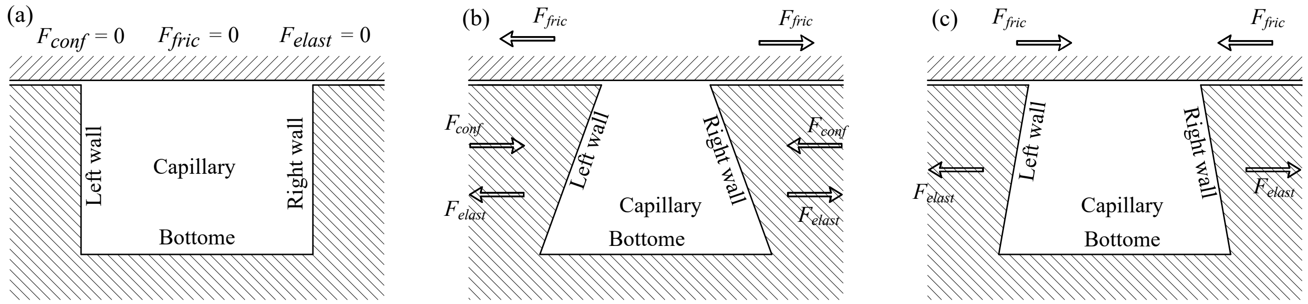

Fig. 9. Schematic diagram of the change in the sample's capillary shape under loading: (a) Unloaded state of the sample, (b) sample under load, and (c) sample unloaded.

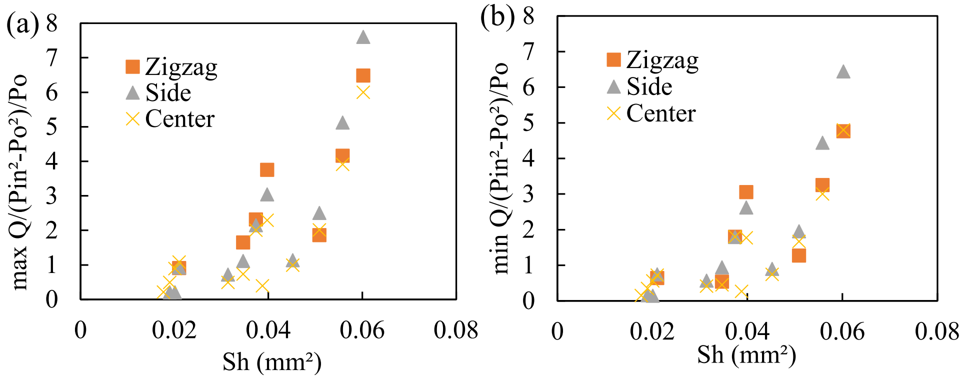

Fig. 10. Dependence of (a) the maximum and (b) minimum conductivity of the samples on the model hydraulic area of the grooves. The types of grooves are indicated by the markers.

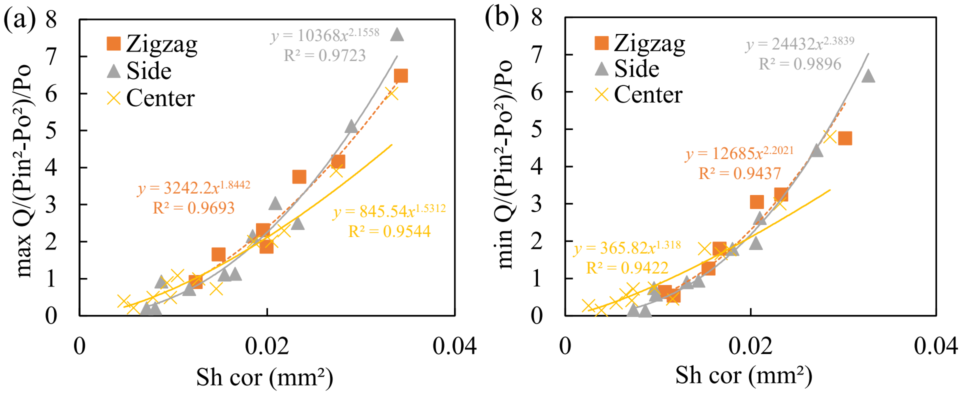

Fig. 11. Dependence of the (a) maximum and (b) minimum conductivity of the samples on the adjusted hydraulic area of the grooves.

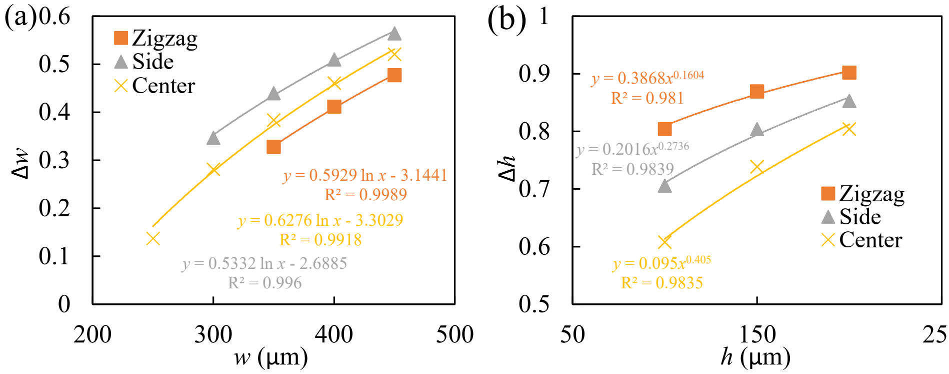

Fig. 12. Dependence of the calculated residual (a) width and (b) residual depth of the grooves after cyclic loading on the initial geometric size.

of the grooves after cyclic loading on the initial geometric size. Fig. 13 shows the dependencies of the exponent n of the power-law equation on the adjusted hydraulic area of the grooves before cyclic loading and after cyclic loading.

3.3 Adjustment of capillary dimensions under cyclic loading

An adjustment of the geometric dimensions of the sample grooves was performed, accounting for the change in their hydraulic resistance under cyclic loading. To assess the correctness of the adjustment, the value of the pressure differential between the inlet and outlet of the sample during nitrogen injection was used. The pressure differential for the flow is a function of velocity, area, and flow regime:

$$\frac{P_{\text{in}}^2 - P_o^2}{P_o} = f(\vartheta, S) \tag{5}$$

where S is cross-sectional area, m^2; ϑ stands for velocity, m/s; P_{in} and P_o are pressures at the inlet and outlet of the sample, Pa. The flow velocity is determined by the nitrogen flow rate and the hydraulic area of the capillary. The Reynolds number Re is a dimensionless quantity characterizing the ratio of inertial forces to viscous friction forces:

$$\text{Re} = \frac{\rho \vartheta D_h}{\mu} = \frac{\vartheta D_h}{\nu} = \frac{Q D_h}{\nu S} \tag{6}$$

where μ and ν are dynamic, Pa·s; and kinematic (m^2/s) viscosities, which depends on pressure differential and temperature. The experimental conditions were isothermal, and the pressure differential varied from 6 to 37 kPa (depending on the capillary conductivity). The hydraulic diameter of a rectangular channel is calculated using the formula:

$$D_h = \frac{2wh}{w+h} \tag{7}$$

For a correct assessment of the pressure differential at a measured conductivity, it is necessary to account for the frictional pressure losses, which are determined by the Darcy-Weisbach equation:

$$dP = \Delta P_f = \lambda \frac{L}{D_h} \frac{\vartheta^2}{2} \rho \tag{8}$$

It can be seen from Eq. (6) that capillary deformation affects the friction factor λ, the hydraulic diameter D_h and the flow velocity ϑ. The adjusting parameters are the capillary width w and depth h. A power-law dependence of the capillary width w and depth h on the confining pressure was chosen as the adjustment function. The results of the adjustment and a comparison of the actual pressure differential dP_{fact}, measured on the filtration setup, with the calculated pressure differential dP_{calc} assuming a constant capillary area, and the adjusted pressure differential dP_{cor}, which accounts for the adjusted hydraulic area of the grooves, are presented in the graphs in

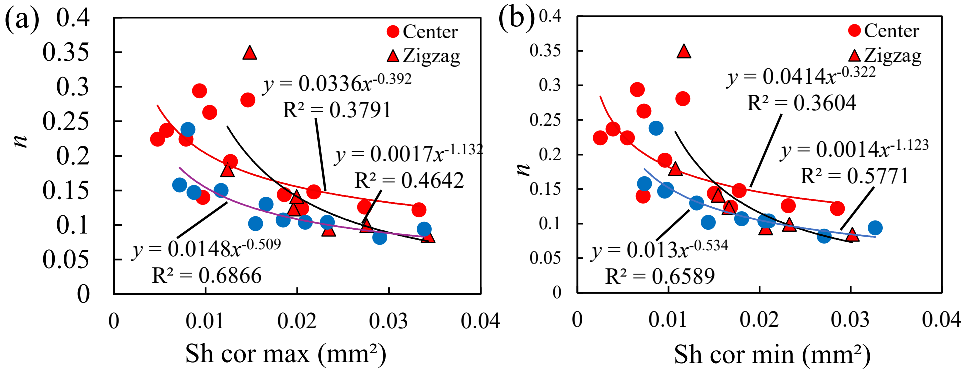

Fig. 13. Dependencies of the exponent n of the power-law equation on the adjusted hydraulic area of the grooves before (a) cyclic loading and (b) after cyclic loading.

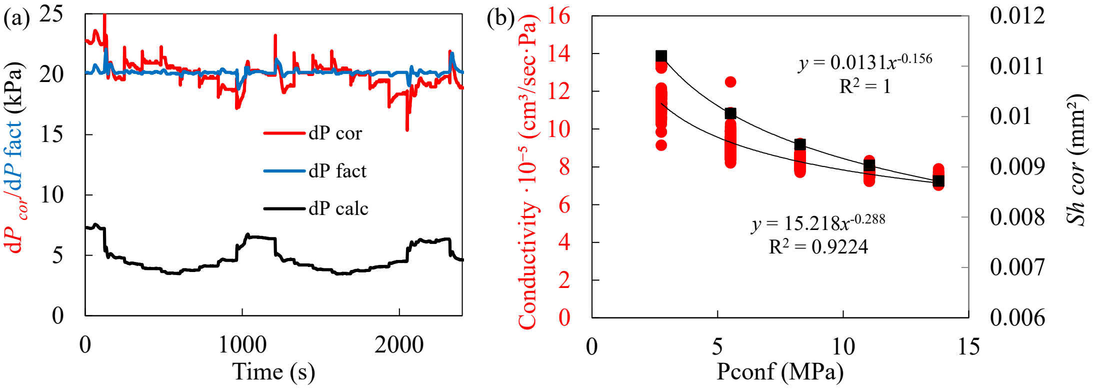

Fig. 14. Laboratory data of cyclic loading: (a) Dynamics of the pressure differential in the samples; (b) dependencies of conductivity (red dots) and the adjusted hydraulic area S_h of the capillary (black squares) on the confining pressure.

Fig. 14 for $w = 250$ μm, $h = 200$ μm (see Appendix for the whole w-h combinations). The adjustment functions for groove width (w_{cor}/w) and depth (h_{cor}/h) are presented in the graphs (Fig. 15).

Based on the adjustment functions for the geometric dimensions of the grooves, it has been mathematically confirmed that under confining pressure, the capillary deforms primarily along the contact plane due to the sliding of the sample's halves against each other. The capillary width is more sensitive to confining pressure. The exponents of the power-law equations describing the width change have a greater magnitude (e.g., -0.094 in Fig. 15(a)) compared to the exponents for the capillary depth (e.g., -0.06 in Fig. 15(a)). The obtained values of the width and depth correction factors allow for predicting changes in the filtration resistance of the grooves.

The accuracy of the obtained adjustment functions in Fig. 15 was verified using the classical power-law equation for sample conductivity (permeability) versus confining pressure under cyclic loading:

$$k = k_o P_{conf}^{-n} \tag{9}$$

where k_o stands for initial conductivity, $\mathrm{cm}^3/(\mathrm{s} \times \mathrm{Pa})$; k stands for actual conductivity, $\mathrm{cm}^3/(\mathrm{s} \times \mathrm{Pa})$; P_{conf} is confining pressure (Pa); n is the exponent characterizing the sensitivity of the sample's conductivity to the confining pressure. Based on the results of the experimental and analytical analysis, it was established that the sample conductivity is sensitive to the capillary area $S_{h\ cor}$. Therefore, the exponent n in Eq. (7) should also depend on the capillary area $S_{h\ cor}$. To verify this, the sample conductivity k and the capillary area $S_{h\ cor}$ were normalized relative to the confining pressure P_{conf}. An iterative variation of the variable (capillary area $S_{h\ cor}$) in Eq. (7) showed (Fig. 16) that the sample conductivity increases with increasing capillary area.

Since the exponent n of the power-law Eq. (7) has a linear dependence on the actual (adjusted) capillary area, it can be confidently stated that the proposed mechanism for changes in capillary conductivity in cylindrical samples under confining pressure is valid.

4. Conclusions

This study conducted experimental investigations into the influence of capillary deformation in cylindrical samples of rock plug size on their hydraulic conductivity. Capillary deformation was studied using 3D-printed samples fabricated from polyurethane via SLA technique. Based on numerous laboratory experiments involving cyclic loading (compaction) of samples and fluid (gas) flow, the influence of the capillary's location and configuration within the sample on capillary conductivity was examined. Changes in conductivity were recorded based on the pressure differential between the sample's inlet and outlet. Based on the results obtained, the foll-

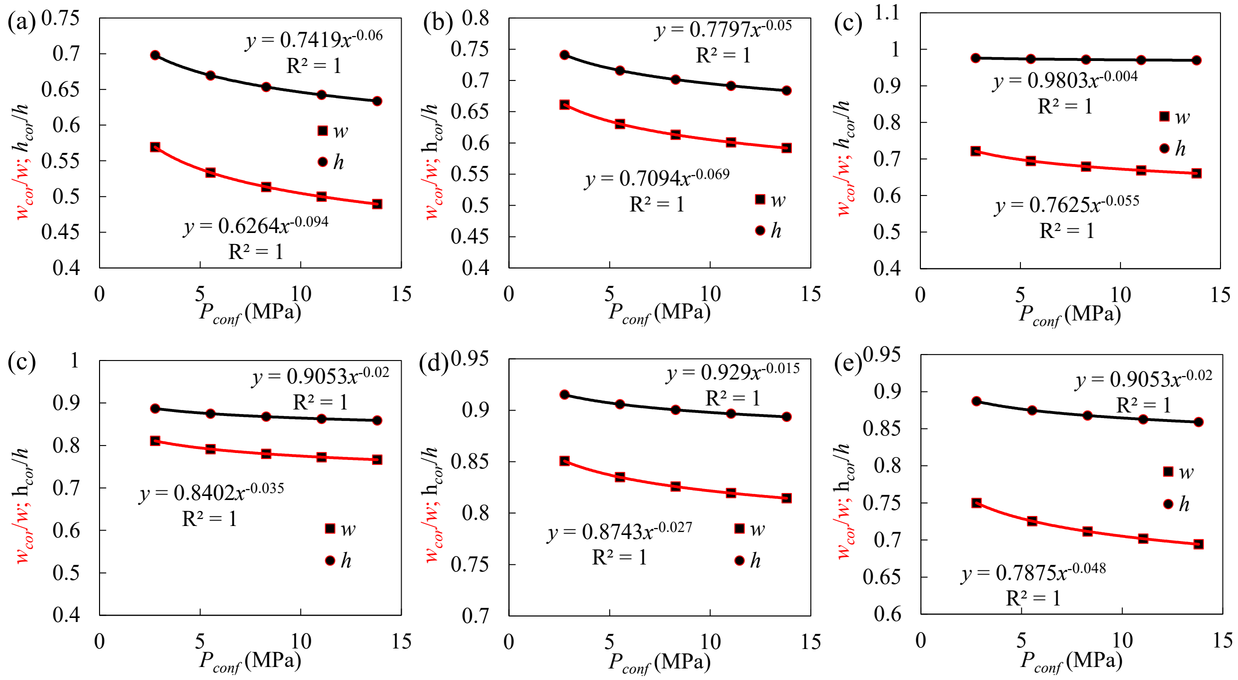

Fig. 15. Adjustment functions for the geometric dimensions of the grooves under cyclic loading for combinations of w and h: (a) $w = 250$ μm, $h = 200$ μm; (b) $w = 300$ μm, $h = 100$ μm; (c) $w = 300$ μm, $h = 150$ μm, side groove ; (d) $w = 300$ μm, $h = 150$ μm; (e) $w = 350$ μm, $h = 150$ μm, side groove and (f) $w = 400$ μm, $h = 150$ μm.

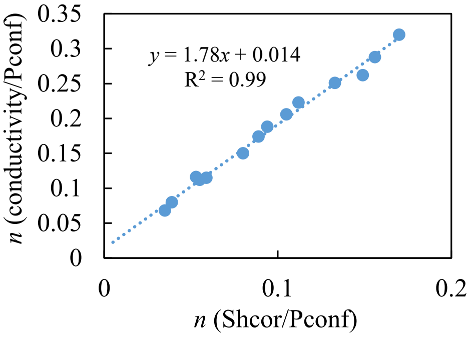

Fig. 16. Dependence of conductivity sensitivity on the indicator of capillary area change under cyclic loading.

owing conclusions can be drawn:

1) If the material contains fluid-conducting capillaries, cyclic loading leads to the deformation of these capillaries, resulting in increased hydraulic resistance (friction factor) and reduced material conductivity;
2) Capillary deformation manifests as a change in its geometric dimensions (height and width), i.e., the crushing of the capillary banks is observed, leading to a reduction in the capillary's hydraulic area, which causes a decrease in sample conductivity which has an incomplete hysteresis;
3) The exponent in the conductivity (permeability) equation for samples under cyclic loading is determined by the hydraulic area of the capillary.

Acknowledgements

The authors would like to acknowledge the generous financial support provided by the Russian Science Foundation (No. 23-19-00699).

Additional information: Author's email

yuliyuan@cumt.edu.cn (L. Yu).

Supplementary file

https://doi.org/10.46690/capi.2025.12.03

Conflict of interest

The authors declare no competing interest.

References

Aghajani, M., Maruf, S. H., Wang, M., et al. Relationship between permeation and deformation for porous membranes. Journal of Membrane Science, 2017, 526: 293-300.

Al Mteiri, S., Suboyin, A., Rahman, M. M., et al. Hydraulic fracture propagation and analysis in heterogeneous middle eastern tight gas reservoirs: Influence of natural fractures and well placement. ACS Omega, 2020, 6(1): 799-815.

Almubarak, M., Germaine, J. T., Einstein, H. H. Fracturing processes in specimens with internal vs. throughgoing flaws: An experimental study using 3D printed materials. Rock Mechanics and Rock Engineering, 2024.

Yang, L., Wang, S., Cai, J., et al. Main controlling factors of fracturing fluid imbibition in shale fracture network. Capillarity, 2018, 1(1): 1-10.

Azin, R., Kazemi, F., Hosseini, S. T., et al. 3D-printed synthetic core plugs: Advancing laboratory simulations for enhanced oil recovery. Results in Engineering, 2025, 26: 105077.

Bandis, S. C., Lumsden, A. C., Barton, N. R. Fundamentals of rock joint deformation. International Journal of Rock Mechanics and Mining Sciences & Geomechanics Abstracts, 1983, 20(6): 249-268.

Bo, M. W., Arulrajah, A., Horpibulsuk, S., et al. Laboratory measurements of factors affecting discharge capacity of prefabricated vertical drain materials. Soils and Foundations, 2016, 56(1): 129-137.

Boro, H., Rosero, E., Bertotti, G. Fracture-network analysis of the Latemar Platform (northern Italy): Integrating outcrop studies to constrain the hydraulic properties of fractures in reservoir models. Petroleum Geoscience, 2014, 20(1): 79-92.

Chen, S., Zhang, J., Yin, D., et al. Visualizing experimental investigation on gas-liquid replacements in a microcleat model using the reconstruction method. Deep Underground Science and Engineering, 2023, 2(3): 295-303.

Dawson, M. A., Germaine, J. T., Gibson, L. J. Permeability of open-cell foams under compressive strain. International Journal of Solids and Structures, 2007, 44(16): 5133-5145.

Eschweiler, J., Horn, N., Rath, B., et al. The biomechanics of cartilage-an overview. Life, 2021, 11(4): 302.

Fan, T., Song, X., Wu, S., et al. A mathematical model and numerical simulation of waterflood induced dynamic fractures of low permeability reservoirs. Petroleum Exploration and Development, 2015, 42(4): 541-547.

Feng, P., Ma, H., Wang, J., et al. Influence mechanism of confining pressure on the hydraulic aperture based on the fracture deformation constitutive law. Frontiers in Earth Science, 2023, 10: 968696.

Gehne, S., Benson, P. M. Permeability enhancement through hydraulic fracturing: laboratory measurements combining a 3D printed jacket and pore fluid over-pressure. Scientific Reports, 2019, 9(1): 12573.

Goodman, R. E. Introduction to Rock Mechanics. New York, USA, 1989.

Goodman, R. The mechanical properties of joints. Paper Presented at the Third International Congress International Society for Rock Mechanics, Denver, Colorado, 1-7 September, 1974.

Hofmann, H., Blöcher, G., Milsch, H., et al. Transmissivity of aligned and displaced tensile fractures in granitic rocks during cyclic loading. International Journal of Rock Mechanics and Mining Sciences, 2016, 87: 69-84.

Ibrahim, E. R., Jouini, M. S., Bouchaala, F., et al. Simulation and validation of porosity and permeability of synthetic and real rock models using three-dimensional printing and digital rock physics. ACS Omega, 2021, 6(47): 31775-31781.

Kamal, M. A., Rabie, M. H., Hussein, H. M., et al. Numerical and field study of wick drains performance in soft clay. Innovative Infrastructure Solutions, 2025, 10(5): 193.

Ketova, Yu.A. Relevant directions in development of polymer compositions for conditions of operated in Perm region reservoirs. Perm Journal of Petroleum and Mining Engineering, 2017, 16(4): 342-349.

Khetabi, E. M., Bouziane, K., Zamel, N., et al. Effects of mechanical compression on the performance of polymer electrolyte fuel cells and analysis through in-situ characterisation techniques-A review. Journal of Power Sources, 2019, 424: 8-26.

Kim, H. M., Inoue, J. Analytical approach for anisotropic permeability through a single rough rock joint under shear deformation. Journal of Geophysical Research, 2003, 108(B8): 2366.

Kluge, C., Blöcher, G., Hofmann, H., et al. The stress-memory effect of fracture stiffness during cyclic loading in low-permeability sandstone. Journal of Geophysical Research: Solid Earth, 2021, 126(10): e2020JB021469.

Kozhevnikov, E. V., Turbakov, M. S., Riabokon, E. P., et al. Cyclic confining pressure and rock permeability: Mechanical compaction or fines migration. Heliyon, 2023, 9(11): e21600.

Kozhevnikov, E., Turbakov, M., Riabokon, E., et al. Rock permeability evolution during cyclic loading and colloid migration after saturation and drying. Advances in Geo-Energy Research, 2024, 11(3): 208-219.

Kozhevnikov, E., Turbakov, M., Riabokon, E., et al. Effect of load vector orientation on uniaxial compressive strength of 3D photoresin. Journal of Manufacturing and Materials Processing, 2025, 9(1): 23.

Kuganeswaran, N., Rahim, A., Ali, N. Consolidation in soft soil-case study on prefabricated vertical drains (PVDs). The Open Civil Engineering Journal, 2021, 15(1): 310-319.

Ma, K., Wang, S., Zhang, L., et al. A microfluidic study on the influence of naturally fractured porous media on the phase behavior of condensate gas depletion. Natural Gas Industry B, 2025, 12(4): 432-446.

Ouf, M., Jørgensen, P. R., Mosthaf, K., et al. Estimation of effective fracture aperture in glacial tills by analysis of dye tracer penetration. Groundwater, 2024, 63(1): 25-40.

Paluszny, A., Matthai, S. K. Impact of fracture development on the effective permeability of porous rocks as determined by 2-D discrete fracture growth modeling. Journal of Geophysical Research: Solid Earth, 2010, 115(B2): B02203.

Persson, K. M., Gekas, V., Trägårdh, G. Study of membrane compaction and its influence on ultrafiltration water permeability. Journal of Membrane Science, 1995, 100(2): 155-162.

Petitjean, N., Canadas, P., Royer, P., et al. Cartilage biomechanics: From the basic facts to the challenges of tissue engineering. Journal of Biomedical Materials Research Part A, 2022, 111(7): 1067-1089.

Planas-Paz, L., Lammert, E. Mechanical forces in lymphatic vascular development and disease. Cellular and Molecular Life Sciences, 2013, 70(22): 4341-4354.

Poplygin, V., Dieng, A., Shi, X. Forecasting hydraulic fracturing results using information amount theory. Perm Journal of Petroleum and Mining Engineering, 2024, 24(2): 93-100.

Rong, G., Huang, K., Zhou, C. A new constitutive law for the nonlinear normal deformation of rock joints under normal load. Science China Technological Sciences, 2011, 55(2): 555-567.

Sun, G. Z., Lin, W. Z. The compressional deformation law of rock mass structure surface and a constitutive equation of rock mass elastic deformation. Chinese Journal of Geology, 1983, 18(2): 177-180.

Tran-Nguyen, H. H., Edil, T. B., Schneider, J. A. Effect of deformation of prefabricated vertical drains on discharge capacity. Geosynthetics International, 2010, 17(6): 431-442.

Vogler, D., Amann, F., Bayer, P., et al. Permeability evolution in natural fractures subject to cyclic loading and Gouge formation. Rock Mechanics and Rock Engineering, 2016, 49(9): 3463-3479.

Wang, G., Liu, Y., Huang, Q., et al. Experimental study on the influence of coal fracture surface roughness on water injection seepage. ACS Omega, 2022, 7(36): 32679-32689.

Wei, J., Shang, D., Zhao, X., et al. Experimental study on production characteristics and enhanced oil recovery during imbibition and huff-n-puff injection in shale reservoir. Capillarity, 2024, 12(2): 41-56.

Witherspoon, P. A., Wang, J. S. Y., Iwai, K., et al. Validity of cubic law for fluid flow in a deformable rock fracture. Water Resources Research, 1980, 16(6): 1016-1024.

Xue, R., Chang, Y., Wang, S., et al. Pore-scale microfluidic investigation of unsaturated CO_2 bubble morphology and interface evolution during drainage-imbibition cycles. Capillarity, 2025, 15(3): 74-86.

Xue, R., Chang, Y., Wang, S., et al. A new fracture permeability model: Influence of surrounding rocks and matrix pressure. Journal of Petroleum Science and Engineering, 2020, 193: 107320.

Zhou, J., Luo, L., Yu, L., et al. Experimental study about the influence of cyclic load on the hydraulic conductivity of clay. Acta Geotechnica, 2020, 15(12): 3357-3370.

Zuo, J., Chen, Y., Liu, X. Crack evolution behavior of rocks under confining pressures and its propagation model before peak stress. Journal of Central South University, 2019, 26(11): 3045-3056.